Journal of the Meteorological Society of Japan, Vol. 92, No. 3, pp. 189–205, 2014
DOI:10.2151/jmsj.2014-301

Numerical Simulation on Retrieval of Meso-γ Scale Precipitable Water Vapor Distribution with the Quasi-Zenith Satellite System (QZSS)

Masanori OIGAWA, Eugenio REALINI

Research Institute for Sustainable Humanosphere, Kyoto University, Kyoto, Japan

Hiromu SEKO

Meteorological Research Institute, Tsukuba, Japan
Japan Meteorological Agency, Tokyo, Japan

and

Toshitaka TSUDA

Research Institute for Sustainable Humanosphere,Kyoto University, Kyoto, Japan

(Manuscript received 19 September 2013, in final form 26 November 2013)

Abstract

A simulation study was conducted to investigate the retrieval of meso-γ scale precipitable water vapor (PWV) distribution with the Quasi-Zenith Satellite System (QZSS) using output from a non-hydrostatic model (JMA NHM). The evaluation was performed on PWV values obtained by simulating three different methods: using all GPS satellites above an elevation angle higher than 10° (PWV_G) (conventional Global Navigation Satellite System (GNSS) meteorology method), using only the QZSS satellite at the highest elevation (PWV_Q), and using only the GPS satellite at the highest elevation (PWV_{HG}).

The three methods were compared by assuming the vertically integrated water vapor amounts of the model as true PWV. As a result, the root mean square errors of PWV_G, PWV_Q, and PWV_{HG} were 2.78, 0.13, and 0.59 mm, respectively, 5 min before the rainfall. The time series of PWV_{HG} had a large discontinuity (~ 2 mm) when the GPS satellite with the highest elevation changed, while that of PWV_Q was small because the elevation at which the highest QZSS satellites change was much higher. The standard deviation of PWV_Q was smaller than those of PWV_G and PWV_{HG}, which vary significantly depending on GPS satellite geometry.

When the spatial distributions of PWV_G and PWV_Q were compared to the meso-γ scale distribution of the reference PWV, PWV_G smoothed out the PWV fluctuations, whereas PWV_Q captured them well, due to the higher spatial resolution achievable using only high-elevation slant paths. These results suggest that meso-γ scale water vapor fluctuations associated with a thunderstorm can be retrieved using a dense GNSS receiver network and analyzing PWV from a single high-elevation GNSS satellite. In this study, we focus on QZSS, since this constellation would be especially promising in this context, and it would provide nearly continuous PWV observations as its highest satellite changes, contrary to using the highest satellites from multiple GNSS constellations.

Keywords precipitable water vapor; Quasi-Zenith Satellite System; thunderstorm; non-hydrostatic model

Corresponding author: Masanori Oigawa, Research Institute for Sustainable Humanosphere, Kyoto University, Gokasho, Uji, Kyoto 611-0011, Japan
E-mail: masanori_ohigawa@rish.kyoto-u.ac.jp

1. Introduction

Water vapor plays an important role for the growth of intense moist convection because it releases significant quantities of latent heat by condensation and

intensifies deep convection, which causes hazardous heavy rainfall. An increase of water vapor in the lower troposphere causes large convective instability of the atmosphere. Therefore, it is important for the mitigation of weather disasters to observe water vapor distributions associated with local heavy rainfall. The GPS meteorology technique is now attracting attention as a method for measuring water vapor fluctuations prior to the initiation of deep convection.

Global Navigation Satellite Systems (GNSS), represented by GPS, are widely used for the precise determination of coordinates. The path length of GPS radio signals is estimated by measuring the travel time of carrier waves transmitted from GPS satellites to receiving antennas. However, propagation delays of GPS signals caused by refraction occur within the atmosphere, which introduce positioning errors. The relation between refractivity (n) and atmospheric parameters, such as temperature (T), partial pressure of dry air (P_d), and partial pressure of water vapor (e), is formulated as follows (Thayer 1974),

$$n-1=10^{-6}\left(k_1\frac{p_d}{T}+k_2\frac{e}{T}k_3\frac{e}{T^2}\right) \quad (1)$$

where k_1, k_2, and k_3 are experimentally determined constants. The atmospheric delay can be calculated by integrating $n-1$ along the ray path, and this value contains information about the amount of accumulated water vapor along the path. Slant tropospheric delays from all the available satellites are mapped onto the zenith direction to estimate the zenith tropospheric delay (ZTD), assuming homogeneous distribution of atmospheric delays around the receiver (MacMillan 1995). ZTD is then converted to PWV, which is the vertically integrated water vapor amount by using surface pressure and temperature at the receiver location (Bevis et al. 1992; Rocken et al. 1993). GPS-derived PWV can be estimated as the spatially averaged water vapor amount within an inverse cone defined by the elevation cutoff angle used for the processing of GPS observations, which is 10°–15° in conventional analysis (Fig. 1).

It has been verified that water vapor maps and their variations associated with weather disturbances can be observed by GPS station networks (Elgered et al. 1997; Iwabuchi et al. 1997). The Geospatial Information Authority of Japan is operating a nationwide GPS observation network in Japan, called the GPS Earth Observation Network System (GEONET) for the real-time monitoring of crustal movement. GEONET consists of about 1300 GNSS stations and has a horizontal resolution of about 20 km. GEONET has also been used to observe water vapor variations through the GPS meteorology project of Japan (Tsuda et al. 1998). The assimilation of GPS-derived PWV on numerical weather prediction (NWP) models can improve the prediction accuracy of heavy rainfall (Kuo et al. 1993; Smith et al. 2000; Gendt et al. 2004; Gutman et al. 2004). Impact studies on the assimilation of GEONET-derived PWV in meso-scale NWP models have also been extensively performed, and the feasibility of using GEONET-derived PWV as assimilation data has been verified. For example, Seko et al. (2004a) and Kawabata et al. (2007) assimilated water vapor data, i.e., GEONET-derived PWV and slant water vapor (SWV), and radial wind velocities of Doppler radar by using four-dimensional variational data assimilation systems, and they noted that the assimilation of these data improved the prediction of precipitation. The Japan Meteorological Agency (JMA) started to use GEONET-derived PWV for operational meso-scale analysis since 2009 (Ishikawa 2010).

However, the monitoring of PWV fluctuations on a scale smaller than GEONET is needed because the numerical prediction of localized heavy rainfall caused by a single cumulonimbus is still difficult, even if the assimilation of GEONET-derived PWV is performed. One probable cause of this problem is that the horizontal scale of a cumulonimbus cloud is as small as a few kilometers; since the spatial resolution of GEONET-derived PWV is 20 km, it is not sufficient to resolve water vapor fluctuations associated with a cumulonimbus cloud. Shoji (2013) introduced the water vapor inhomogeneity index, computed as the standard deviation of higher-order atmospheric inhomogeneity derived from the post-fit phase residuals of GPS analysis, which indicates the degree of inhomogeneity of water vapor on a scale of 2–3 km; this index was shown to increase ahead of the initiation of a convective precipitation event on 11 August 2011. Seko et al. (2004b) studied meso-γ scale water vapor fluctuations associated with a thunderstorm using a dense network of GPS receivers. Seventy-five GPS receivers within an area of 20 × 20 km^2 were used in this GPS observation campaign. They found that the amount of water vapor at 1 km height increased about 20 min before the formation of raindrops of a thunderstorm. The observation of meso-γ scale water vapor fluctuations ahead of the initiation of deep convection is essential for the now-casting and forecasting of localized heavy rainfall, although they have not been captured yet by high-resolution observation.

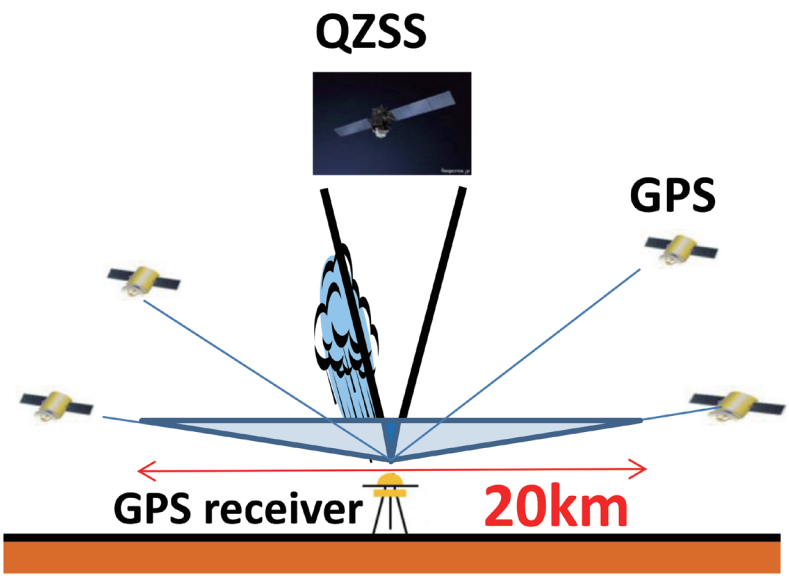

Fig. 1. Schematic illustration of GPS observations. Representativeness of PWV can be improved by using high elevation satellites, like those of QZSS.

Sato et al. (2013) performed high-resolution observations of meso-γ scale water vapor fluctuations associated with local heavy rainfall using a dense network of GNSS receivers. These receivers were installed with a horizontal resolution of about 1–2 km around the Uji campus of Kyoto University, Japan. They noted that GPS-derived PWV estimated by conventional GPS meteorology is too wide to capture meso-γ scale PWV fluctuations because delays from all available GPS satellites above a low elevation angle are averaged to estimate a single value of PWV. To improve the horizontal resolution of PWV, they carried out a preliminary test of PWV estimation that uses a single slant wet delay (SWD) at high elevation. In GNSS processing, the SWD for a target satellite can be estimated as follows (Shoji et al. 2004): (1) estimating the Zenith Total Delay with multiple GNSS satellites; (2) computing the ZWD and mapping it to the line-of-sight of the target satellite by a mapping function (and optionally a tropospheric delay gradient model); (3) adding the correspondent post-fit phase residual, after removing direction-specific errors such as the effects of multi-path and phase center variations, to the mapped slant wet delay obtained in point (2). Although the estimated ZWD may already have biases (with respect to the "true" ZWD), also because of the uneven distribution of GNSS satellites, and these biases propagate to slant delays (Iwabuchi et al. 2004), the ZWD estimated from a single slant delay at a high elevation is expected to be closer to the reference (or "true") ZWD because it includes the direct observation of the water vapor amount close to the zenith direction. Basically, we assume that the local fluctuations of water vapor within the low-elevation inverse cone (i.e., as observed along the various slant paths used for the processing) have a higher magnitude compared to the biases and observation errors; this is expected to be true especially in active weather conditions, which is the main scenario of interest for this study. Studies exist that have investigated the retrieval of PWV from single slant delays estimated by the processing of real observations: Seko et al. (2004b) retrieved a three-dimensional water vapor distribution by using the tomographic method and SWV data. They showed that water vapor distributions estimated using SWV were consistent with radar observation results. Sato et al. (2013) reported that the SWV retrieved along ray paths that were close to radiosonde trajectories had a higher level of consistency with radiosonde-derived PWV than with GNSS-derived PWV retrieved by the standard method. It should be pointed out that also the SWV retrieved from low-elevation slant paths is useful, because it contains water vapor information

at locations distant from the receiver. Some studies assimilated SWV into meso-scale NWP models and reported that the prediction results of heavy rainfall were improved (Seko et al. 2004a; Kawabata et al. 2007). These results suggest that SWV has sufficient accuracy to capture small-scale water vapor inhomogeneity. The estimation of PWV by high-elevation slant paths would be especially effective when a high-elevation QZSS satellite is used, because QZSS satellites can continuously stay over an elevation angle of 80° for about 6 h over Japan, whereas the geometry of GPS satellites is more variable, and timespans may occur during which no satellite higher than 60° is available. The only currently available QZSS satellite is "QZS-1," or "Michibiki," operated by the Japan Aerospace Exploration Agency (JAXA); three more satellites are planned to be launched by 2017–2019; by then, QZSS will provide at least one satellite continuously close to the zenith, at an elevation angle higher than 80° over Japan. By using a dense network of receivers and high-elevation satellites, it is possible to estimate high-resolution maps of water vapor; however, it is difficult to evaluate their accuracy only from the information of observations because comparable independent observations of the water vapor field at high resolution are very limited.

In this study, we present a simulation study performed using the output of a non-hydrostatic numerical model to evaluate the reliability of the spatial distributions of PWV estimated by (1) the conventional GPS meteorology method and (2) by using only a high-elevation satellite. The grid point data of a NWP model is useful because it provides information about the three-dimensional distributions of atmospheric parameters, including the amount of water vapor, and we can calculate SWV values in any azimuth and elevation angle. The horizontal distributions of PWV estimated by mapping SWV values derived from the numerical model were evaluated by comparing them with reference PWV values of the model (estimated by vertically integrating the products of density and water vapor mixing ratio), and the impact of a completed QZSS constellation on the observation of PWV was simulated.

Section 2 describes the non-hydrostatic model used in this study, its experimental design, and three methods according to which we simulated GNSS-derived PWV values from grid point data by a NWP model. Section 3 details the features of a simulated rainfall system that caused meso-γ scale PWV fluctuations in the model. Section 4 describes the time variation and horizontal maps of PWV estimated by the three different methods introduced in Section 2. In Section 5, results are discussed and generalized. Section 6 summarizes and concludes this study.

2. Method

2.1 Non-hydrostatic meso-scale model and design of the simulation

The JMA non-hydrostatic model (JMANHM) (Saito et al. 2007) was used to make the three-dimensional grid point data, which represent atmospheric conditions associated with heavy rainfall. JMANHM used in this study is a fully compressible model, with governing equations that do not contain approximations about the density of the atmosphere, which enable us to treat water vapor amount accurately. This model is the same as that used for operational meso-scale forecast by the JMA. Two different simulations with a horizontal grid interval of 5 km and 1 km, respectively, (from now on: 5-km NHM and 1-km NHM) were performed. The 5-km NHM simulation has 151 × 151 horizontal grid points and a horizontal domain centered at 35°N, 135°E on a Lambert conformal projection; the model domain is shown in Fig. 2a. The 1-km NHM simulation has 451 × 451 horizontal grid points and a horizontal domain centered at 34.9279°N, 134.8418°E on the same projection; the model domain is shown in Fig. 2b. Both 5-km NHM and 1-km NHM have a vertical resolution of 50 levels from the surface to the model top (21801 m). A hybrid terrain following coordinate is adopted as the vertical coordinate. The lowest atmospheric level was 20 m above the surface, and the depth of the layers increased from 40 m to 886 m as their height increased. The initial time of 5-km NHM was 15:00 Local Standard Time (LST) on 28 July 2011, and initial and boundary conditions were set on the basis of JMA meso-scale analysis data (NPD/JMA 2013). 1-km NHM was nested within the output of 5-km NHM, with the initial time set at 16:00 LST on 28 July 2011. Cumulus parameterization used in 5-km NHM followed the Kain–Fritsch scheme with three-ice bulk cloud physics (Kain and Fritsch 1993). In 1-km NHM, only three-ice bulk cloud physics was used, with no cumulus parameterization. The prognostic variables were wind components, temperature, pressure and all water-related quantities such as vapor, rain, clouds, snow, graupel, and ice clouds (all three-dimensional).

2.2 Estimation of PWV from the simulated field

In GPS positioning, unknown parameters such as position coordinates of the receiver antenna, receiver

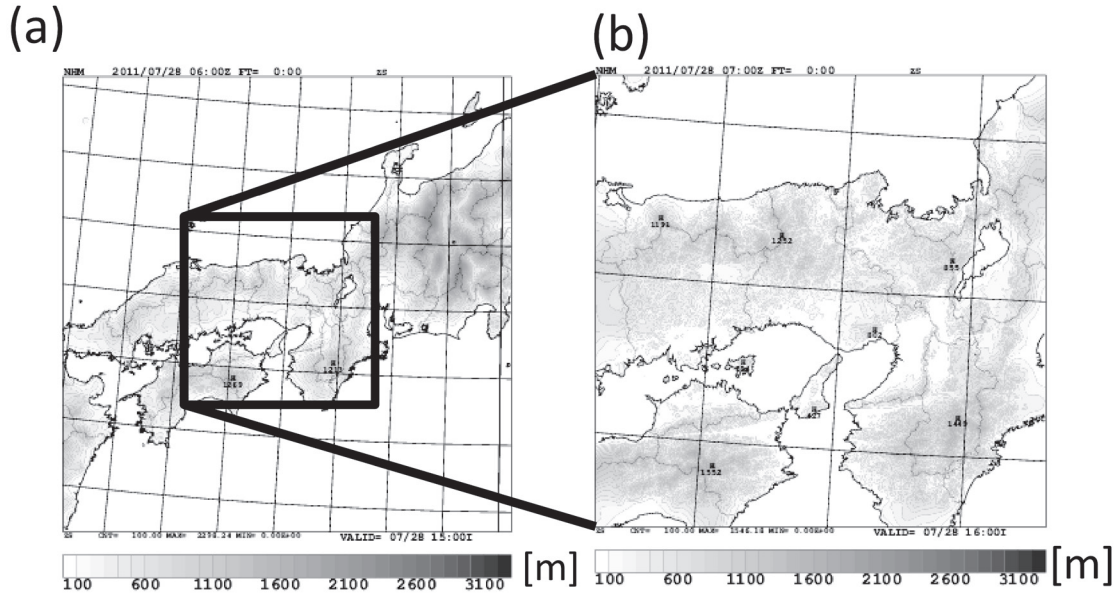

Fig. 2. NHM model domains used for the 5 km grid interval experiment (a) and the 1 km grid interval experiment (b). Shade indicates the altitude of the model surface.

clock offset, and atmospheric delays are estimated by GPS observation processing software. PWV can then be retrieved from the estimated tropospheric delay of the GPS signal. However, GPS-derived PWV can also be simulated from the grid point data of a NWP model: in this case, the simulated PWV and its difference from the "true" value (i.e., the reference PWV value estimated by the NWP model) can be easily calculated because the three-dimensional water vapor distributions are known. In this study, a program used in Seko et al. (2004c) was used to calculate PWV from the output of JMANHM. First, this program converts grid points of NHM output to Cartesian coordinates centered at a receiver point by considering the curvature of the Earth; then, the output model values are interpolated at the new grid points. Second, observed or simulated paths of GNSS signals are introduced using information about satellite azimuth and elevation angles at the receiver position. Although GNSS signals are usually bent by the atmosphere, ray paths are approximated by straight lines (from now on: slant paths) connecting the receiver on the ground to each observed GNSS satellite. Third, values of water vapor mixing ratio are interpolated. In this study, 100-m intervals are used along these slant paths from surrounding grid point values, and then SWV values are calculated by integrating water vapor amounts along the slant path. Finally, PWV values are estimated by mapping SWV values to the zenith direction. In our study, when all SWV values above an elevation angle of 10° were used to estimate PWV, i.e., according to the conventional GPS meteorology technique, these SWV values were mapped by using Niell's wet mapping function (Niell 1996) and a first-order gradient model. Hereafter, we call this value PWV_G. When PWV was retrieved from the slant path of the highest QZSS satellite, a sinθ mapping function was used, where θ is the elevation angle of the path, because Niell's wet mapping function can be approximated by 1/sinθ at a high elevation angle. Hereafter, this PWV value is called PWV_Q. When PWV was retrieved from the slant path of the highest GPS satellite, a sinθ mapping function was also used. Hereafter, this PWV value is called PWV_{HG}. These three types of PWV values were calculated every 5 min. It should be noted that real GNSS processing suffers from various errors such as multipath effects, unmodeled phase center variations, and satellite orbit and clock errors. This is true in particular for precise point positioning (PPP), which is often used for retrieving tropospheric delays (and PWV). The simulated PWV_G, PWV_Q, and PWV_{HG} in this study are a simplification of the correspondent PWV values, which could be obtained by real GNSS processing, in the sense that they do not

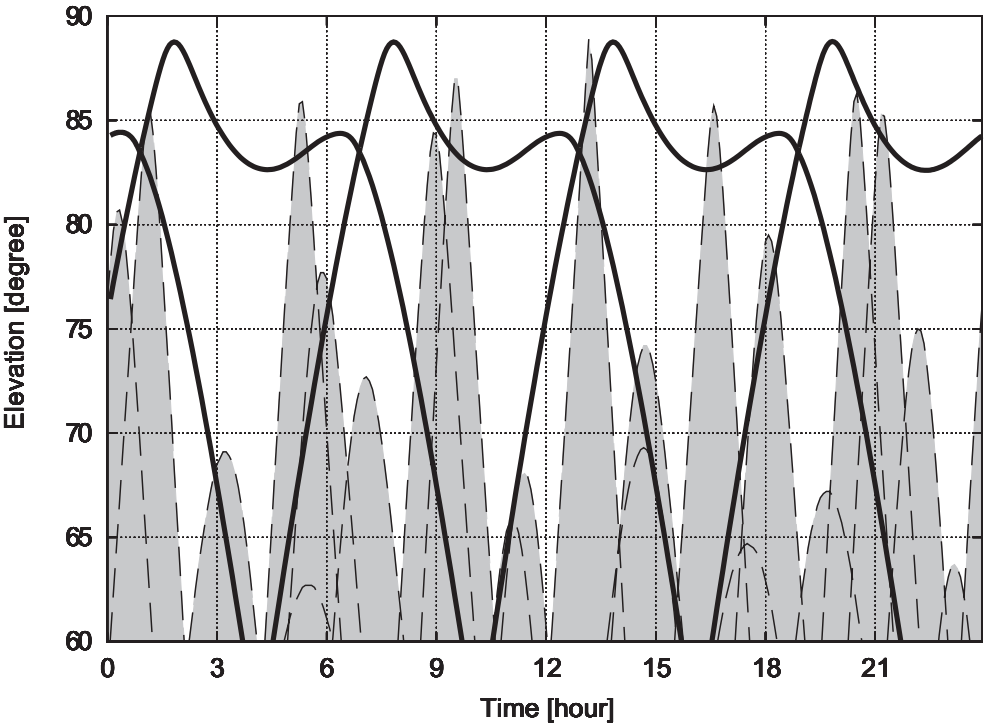

Fig. 3. Time variation of elevation angles of GPS (dashed line) and QZSS (solid line) satellites. Values observed at GEONET station 0347 on 28 July 2011.

attempt to simulate such errors or to introduce specific weighting strategies to mitigate them. However, PWV_G maintains the main characteristics of spatial "averaging" within a low-elevation inverse cone, as opposed to the PWV derived from single slant delays. Since the main objective of this study is to investigate the effects of different slant path geometries on the detection of meso-γ scale water vapor fluctuations, especially by comparing the "averaged" PWV_G and the single slant-derived PWV_Q and PWV_{HG} in a relative sense, we deem this simulation method sufficient for the scope of our investigation.

Figure 3 shows the time variation of elevation angles of GPS and QZSS satellites included in this simulation. The apparent trajectories of GPS satellites used in the simulation are those observed at the 0347 station of GEONET. The apparent trajectories of QZSS satellites are derived from JAXA. Although "Michibiki" is the only QZSS satellite currently available, a constellation of four QZSS satellites was generated, assuming the expected future situation. GPS satellites stay over an elevation angle of 70° only for about 1 h, whereas QZSS satellites continuously stay over an elevation angle of 80° (and each QZSS satellite for more than 6 h).

3. Features of the simulated rainfall system

Figure 4 shows the horizontal distribution of precipitation intensity every 30 min from 16:30 to 18:00 LST simulated by 1-km NHM. The locations of GEONET stations 0347 and 0649 are indicated by triangular and circular marks, respectively. The PWV calculation was performed by assuming that GNSS receivers were located at these two points. In the simulated field of 1-km NHM, a line-shaped rainfall system was generated north of the receiver positions, and torrential rainfall occurred at stations 0347 and 0649. The line-shaped rainfall system was elongated zonally, and the zonal length was about 100 km. At 16:30 LST, the line-shaped rainfall system was located north of stations 0347 and 0649. The rainfall system gained strength as it moved southwards and reached the location of station 0347 at 17:00 LST. It continued to move southwards and reached the location of station 0649 at 17:30 LST. Precipitation intensity over station 0347 became weak at this time. After having passed the 0347 and 0649 station points, the line-shaped rainfall system decayed, and only weak

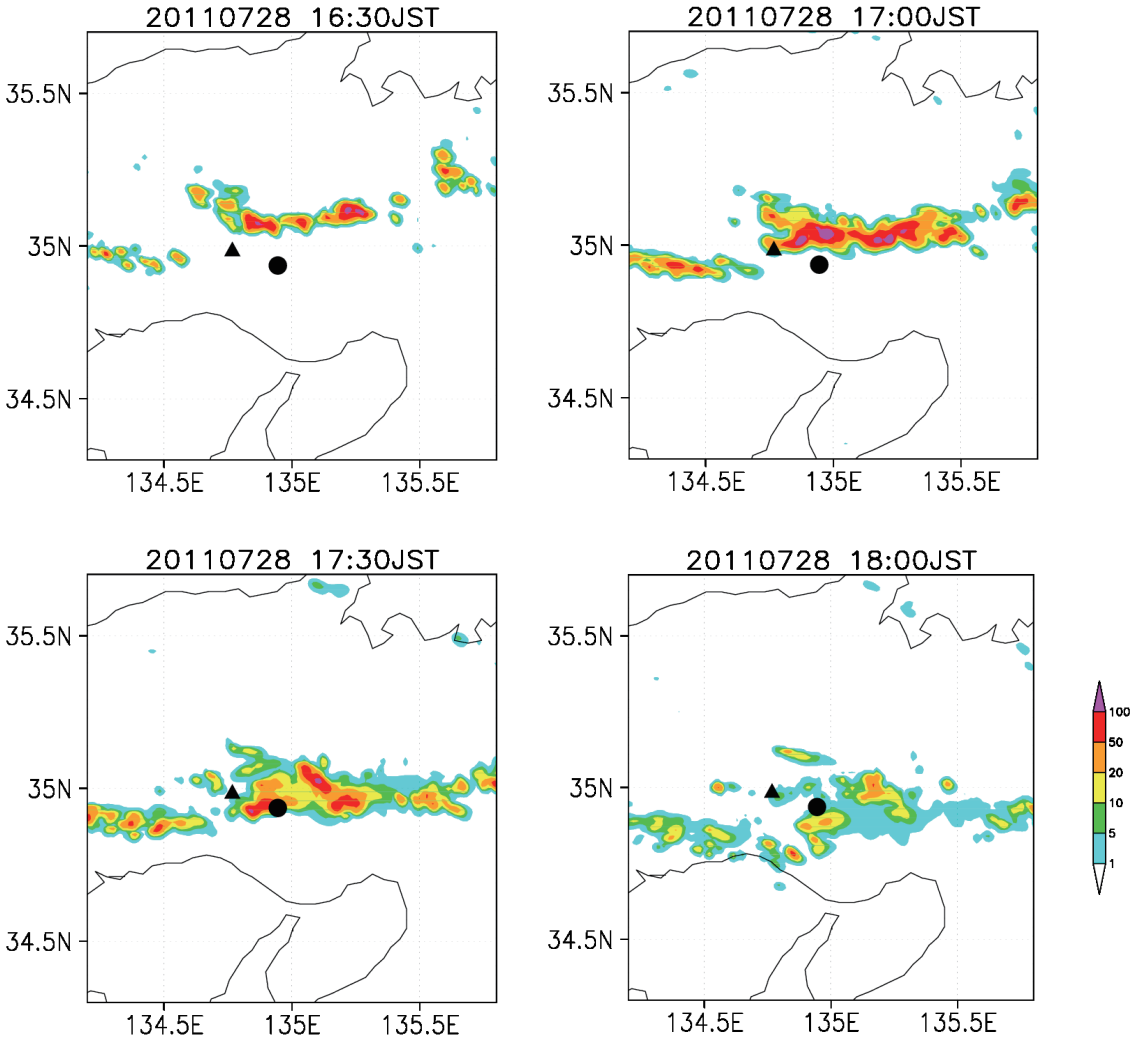

Fig. 4. Horizontal distribution of precipitation intensity (mm h^{-1}) simulated by JMANHM. GEONET station 0347 is indicated by the ▲ mark and station 0649 is indicated by the ● mark.

precipitation was seen near the receiver points at 18:00 LST. The time variation of the three types of PWV values (PWV_G, PWV_Q, PWV_{HG}) associated with this line-shaped rainfall system at stations 0347 and 0649 was calculated.

4. Analysis of the simulated GNSS-derived PWV

4.1 Time variation of the simulated GNSS-derived PWV

Figure 5a shows the time variation of elevation angles of the QZSS and GPS satellites used in this simulation during a timespan ranging from 16:05 LST to 18:30 LST on 28 July 2011. The numbers depicted in the figure are GPS satellite pseudorandom noise (PRN) codes, i.e., unique numbers used to univocally identify each satellite. Hereafter, GPS satellite PRN codes are represented as GPS ID #XX. The replacement of the highest-elevation satellite for QZSS occurred only once at 16:55 LST, whereas it occurred two times for GPS. The highest-elevation satellite of GPS changed from GPS ID #3 to GPS ID #19 at 16:35 LST and from GPS ID #19 to GPS ID #11 at 18:05 LST. The elevation angle of the QZSS satellite with the highest elevation was continuously higher than that of GPS.

The time variation of PWV and precipitation intensity at station 0347 are shown in Fig. 5b. It started raining at 17:00 LST, and intense rainfall continued until 17:25 LST. From 17:40 LST to 18:00 LST, rain-

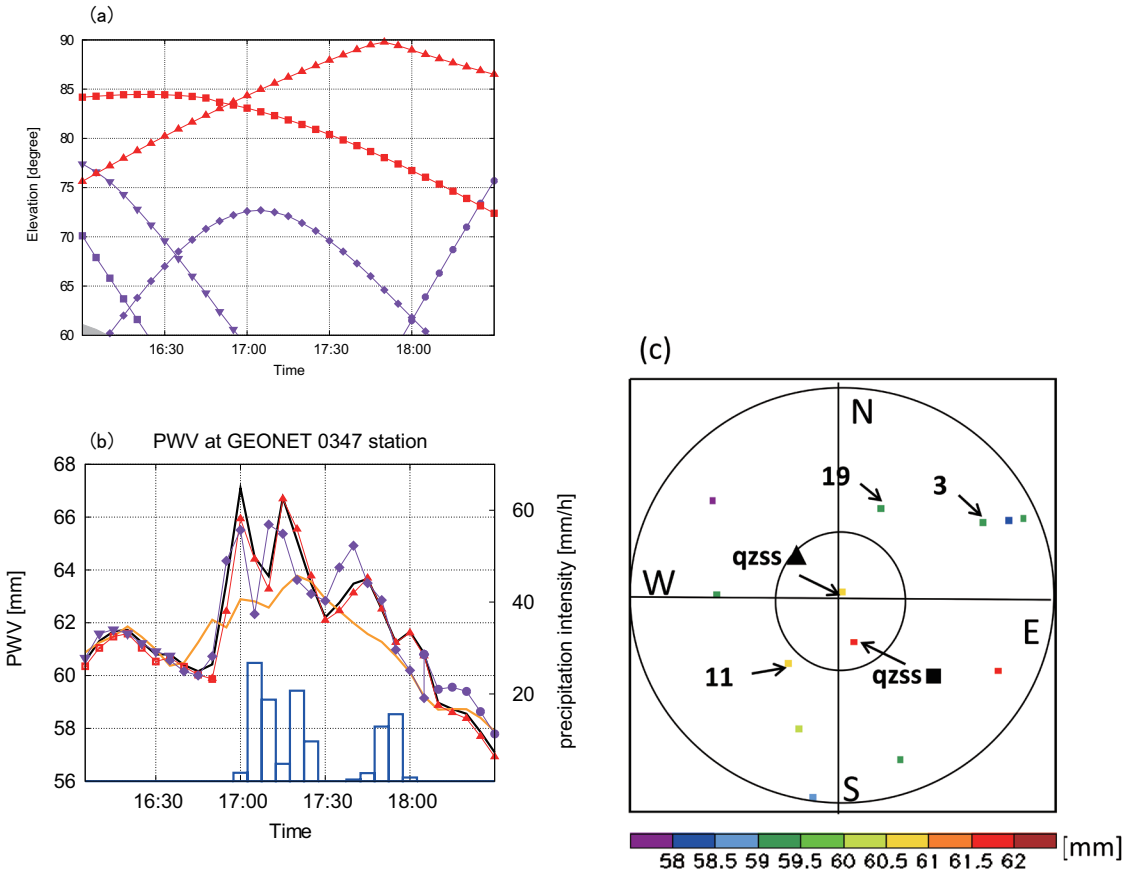

Fig. 5. (a) Time variation of satellite elevation angle of QZSS (red) and GPS (purple). (b) Time variation of PWV (line and marks) and precipitation intensity (bars) at station 0347. The black line and orange line indicate the reference PWV value and PWV_G, respectively. Red and purple marks indicate PWV_Q and PWV_{HG} at station 0347, respectively. Time resolutions are 5 minutes and two values are plotted when replacement of the highest satellite occurred, during the last five minutes. (c) Skyplot of vertical scaled slant total water vapor amount at station 0347 at 18:05 LST.

fall was observed again. The reference PWV value estimated by the NHM model at station 0347 is indicated by the black line. This value started to increase 10 min before the rainfall started and increased by 7 mm within 10 min. PWV_G became larger than the reference value 20 min before it started raining and became smaller than the reference value about 5 min before the rainfall. The root mean square error (RMSE) difference between PWV_G, PWV_Q, and PWV_{HG} time series and the reference PWV time series from 16:45 to 18:05 LST was 1.82 mm, 0.46 mm, and 1.15 mm, respectively. PWV_{HG} was discontinuous at 18:05 LST when the highest-elevation GPS satellite changed from GPS ID #19 to GPS ID #11; this change introduced a variation of about 2 mm in PWV_{HG}. In contrast, the discontinuity observed in PWV_Q as the highest-elevation QZSS satellite changed (16:50 LST) was very small (about 0.03 mm); this is expected, since the QZSS orbit causes satellites to have positions at which the highest-elevation satellite changes closer to the zenith, contrary to GPS.

The skyplot of GPS and QZSS satellites at 18:05 LST is shown in Fig. 5c. Color denotes the vertical-scaled SWV values of each slant path. The positions of the high-elevation satellites shown in Fig. 5a are indicated by arrows (GPS) and triangular and square marks (QZSS). The amount of water vapor increased from the zenith to the south side of station 0347. GPS satellite GPS ID #19 was located north–

northeast of the receiver, whereas GPS satellite GPS ID #11 was located southwest. The difference of vertical-scaled SWV values of these two slant paths was as much as 2 mm. The cause of this discontinuity is that the elevation angles of these two satellites, which were the highest ones for GPS at 18:05 LST, were not so high (about 60°), and their azimuth angle was significantly different; slant paths of GPS ID #19 and GPS ID #11 satellites passed through completely different portions of the atmosphere even if the elevation angles were almost the same. This caused the large discontinuity observed in PWV_{HG} time series. In contrast, when the replacement of the highest-elevation QZSS satellite occurred, the elevation angles of the two satellites were so high that the two slant paths observed almost the same portion of the atmosphere.

To investigate whether PWV variations simulated at the station 0347 can also be calculated at other stations, time variations of PWV and precipitation intensity at station 0649 are shown in Fig. 6a. Rain began at 17:30 LST, and intense rainfall was observed until 17:45 LST. A sharp increase of the reference PWV value occurred 20 min before the rainfall started and increased about 6 mm during 15 min. PWV_G became larger than the reference value about 30 min before the rainfall and then smaller about 10 min before the rainfall. The RMSEs of PWV_G, PWV_Q, and PWV_{HG} time series with respect to the reference time series from 17:00 to 18:30 LST were 1.37 mm, 0.29 mm, and 1.04 mm, respectively. As in the previous case, a discontinuity of PWV_{HG} due to the change of the highest GPS satellite occurred at 18:05, with a PWV_{HG} decrease of about 2 mm. The correspondent discontinuity of PWV_Q was confirmed to be very small (0.05 mm).

Distributions of the vertical-scaled SWV values observed from station 0649 at 18:05 LST are shown in Fig. 6b. Water vapor amounts north of the station were larger than those on the south side, and the vertical-scaled SWV of GPS satellite GPS ID #19 was about 2 mm larger than that of GPS ID #11.

4.2 Spatial analysis of the simulated GNSS-derived PWV based on slant path geometry

Horizontal distributions of water vapor mixing ratio at 3 km height and its vertical cross sections are shown in Fig. 7, with overlaid GNSS slant paths observed at the station 0649. At 16:30 LST, 1 h before the rainfall, differences between the reference PWV value and PWV_G, PWV_Q, and PWV_{HG} were less than 1 mm (Fig. 6a, Table 1). Although there was a humid region (~0.005 kg kg^{-1}) more than 10 km north of the receiver, which might be associated with the rainfall system, the water vapor distribution around the receiver was relatively homogenous. At 17:00 LST, 30 min before the rainfall, PWV_G was overestimated (1.54 mm higher than the reference value), whereas the difference between the reference value and PWV_Q remained small (about 0.30 mm lower). The difference between the reference value and PWV_{HG} doubled (from 0.25 mm to 0.49 mm). The amount of water vapor around station 0649 became larger 30 min before the rain started because the line-shaped rainfall system moved southward and approached the receiver. The overestimation of PWV_G occurred because the low-elevation angle slant path that pointed to the north–west direction passed through the humid region associated with the rainfall system. If one SWV value is significantly larger than that of the other directions, PWV_G is overestimated because it is the result of the averaging of all SWV above an elevation angle of 10° projected to the zenith direction. As seen in Fig. 6a, a rapid increase of PWV_G preceded that of the reference PWV by about 20 min. This time difference may correspond to the time the moist area took to reach the station 0649 from the place at which a low-angle slant path detected it. At 17:25 LST, 5 min before the rainfall, PWV_G was underestimated (3.23 mm lower than the reference value) because the rainfall system reached the station, and the top height of the humid layer over 0.001 kg kg^{-1} was relatively higher just over the location of the receiver due to deep convection; at this time, no GPS slant paths were available at sufficiently high elevation angles to intersect the top height of the humid layer, while some GPS slant paths were passing through less humid zones. In contrast, the difference between the reference PWV value and PWV_Q was quite small (less than 0.1 mm), because the highest-elevation QZSS slant path was close to the zenith direction. At 17:40 LST, 10 min after starting the rainfall, the differences of PWV_G and PWV_Q from the reference value were almost the same; that of PWV_{HG} was the smallest probably because water vapor field over the receiver was so complicated that there was a chance for PWV_{HG} to become more accurate than PWV_Q.

4.3 Horizontal distribution of the simulated GNSS-derived PWV

The horizontal distribution of PWV_G and PWV_Q was calculated by assuming that 49 GNSS receivers were installed in a square area of about 16.4 × 16.7 km^2, with a spatial resolution of 2.7 km along longitudinal and latitudinal lines. The simulated PWV distri-

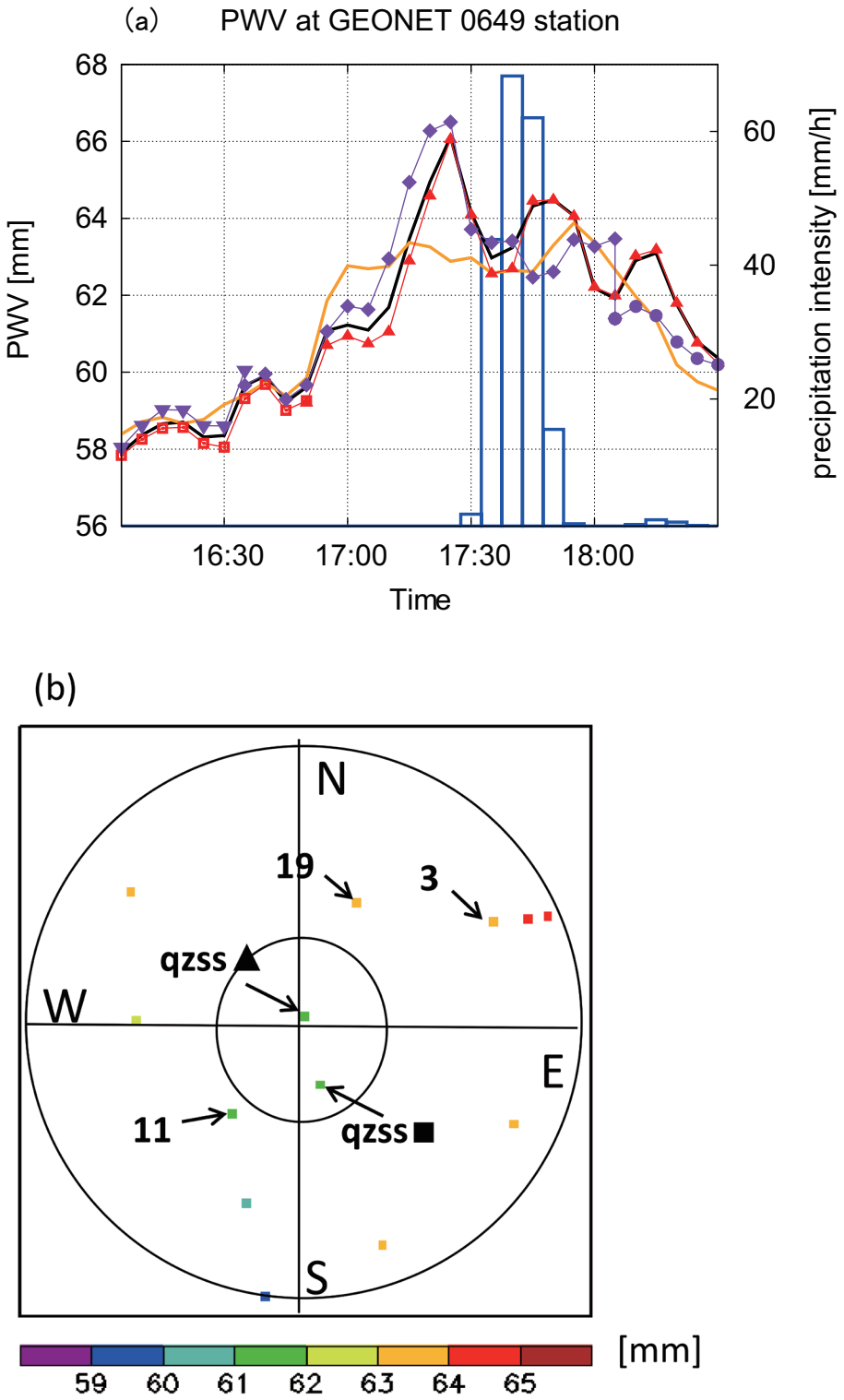

Fig. 6. (a) Same figure as Fig. 5b at station 0649. (b) Same figure as Fig. 5c at station 0649 at 18:05 LST.

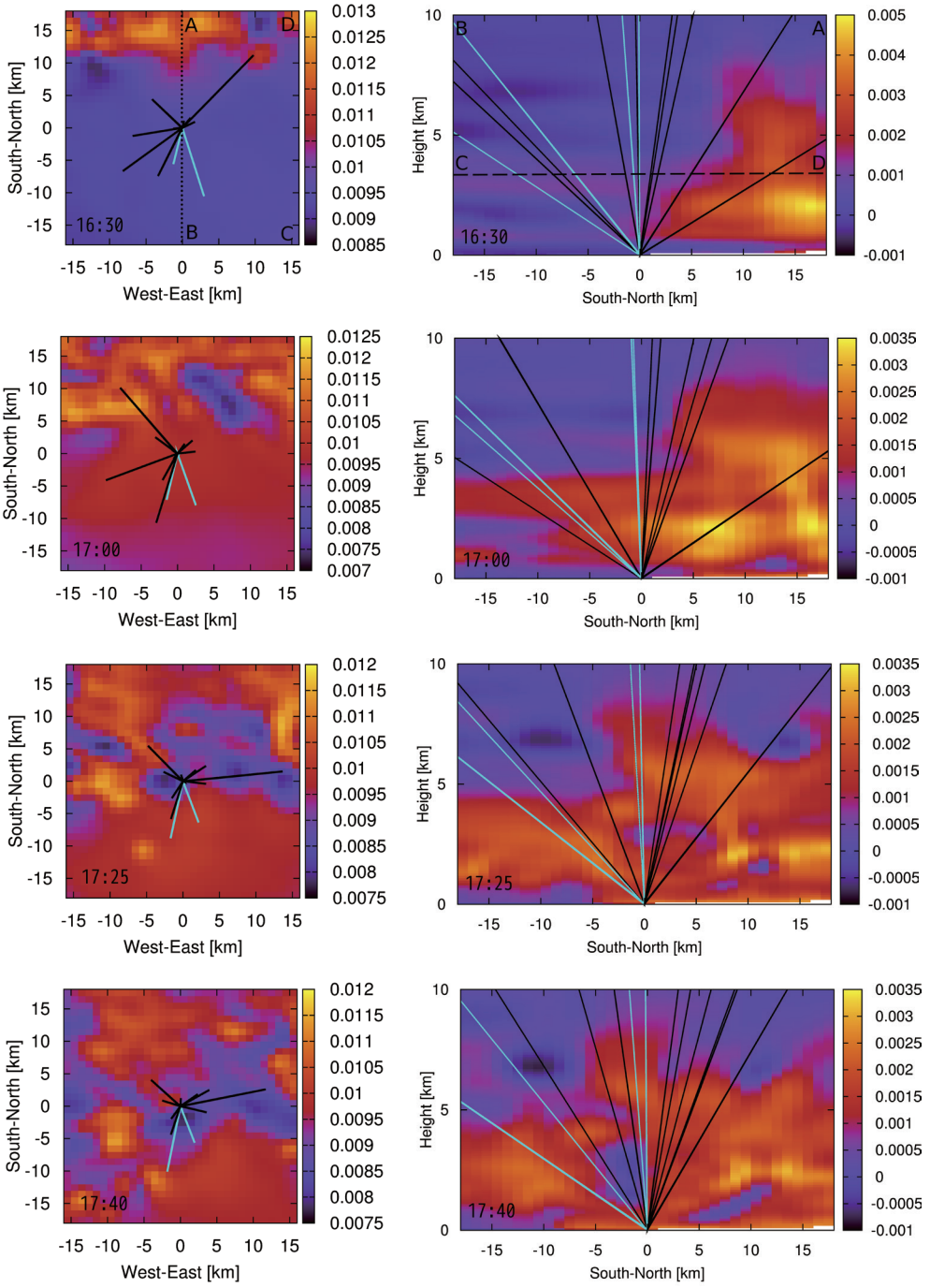

Fig. 7. (Left-side figures) Horizontal distribution of water vapor mixing ratio (kg kg^{-1}) at 3 km height indicated by color shade and ray paths of GNSS radio signals under 3 km height projected to horizontal plane (corresponding to the dashed line C-D on the vertical cross section). Black and blue solid lines indicate the ray paths of GPS and QZSS radio signals, respectively. (Right-side figures) Meridional-vertical cross sections of water vapor mixing ratio indicated by color shade and ray paths of GNSS radio signals projected to this cross section (corresponding to the dotted line A-B on the horizontal plot). Black and blue solid lines indicate the ray paths of GPS and QZSS radio signals, respectively. The value of water vapor mixing ratio shown here is the anomaly from the average at each level.

Table 1. Differences between the true PWV value and the PWV estimated by different estimation method (PWV_G, PWV_Q, PWV_{HG}) at the station 0649 at 16:30, 17:00, 17:25 and 17:40 LST, respectively.

TIME [LST]	16:30	17:00	17:25	17:40
PWV_G [mm]	0.81	1.54	–3.23	–0.59
PWV_Q [mm]	–0.30	–0.29	–0.06	–0.54
PWV_{HG} [mm]	0.25	0.49	0.39	0.18

butions at 17:20 LST near station 0649 are shown in Fig. 8. The rainfall system was over this domain at 17:20 LST (Fig. 8a). The distribution of the reference PWV associated with the intense rainfall is shown in Fig. 8b. The reference PWV value was large in the southwest part of the domain, where the precipitation intensity was about 100 mm h^{-1}. A PWV variability of about 10 mm was observed in this small (meso-γ scale) region.

The simulated distributions of PWV_G and PWV_Q are shown in Figs. 8c and 8d, respectively. Fluctuations observed in the reference PWV value associated with the heavy rainfall were smoothed out by PWV_G, while PWV_Q captured them accurately. The absolute difference of PWV_G and PWV_Q from the reference value is shown in Figs. 8e and f, respectively. The difference of PWV_G from the reference value was large from the southwestern part to northeastern part of the domain, where the rainfall intensity is strong, and the reference PWV values are large. This result suggests that meso-γ scale water vapor fluctuations associated with a thunderstorm could not be captured by PWV_G. As mentioned before, the horizontal distribution of PWV_G is smoothed because all the slant information above an elevation angle of 10° are mapped to zenith and averaged. Thus, PWV_G is not appropriate for high-horizontal-resolution PWV observation with inter-station distances equal to or shorter than 2.7 km. In contrast, PWV_Q captured meso-γ scale water vapor fluctuations associated with a thunderstorm. The scale height of water vapor is defined as the height at which the water vapor amount becomes $1/e$ times that at the surface; about 63 % of PWV is included under this height, assuming an exponential decrease of the water vapor amount. We calculated the scale height of water vapor from the NHM output by spatially and temporally averaging within an area of 20×20 km^2 around the 0649 station from 17:00 LST to 18:00 LST; the result was 2.75 km. Therefore, if we assume that GNSS-derived PWV represents the water vapor amount within an inverse cone defined by the elevation cutoff used for the processing of GPS observations (Fig. 1), and elevation cutoffs of PWV_G and PWV_Q are 10° and 80° respectively, the spatial resolutions of PWV_G and PWV_Q are estimated as about 30 km and 1 km, respectively. To verify the validity of this estimation, PWV_G and PWV_Q values at the station 0649 were compared with the areal average of the reference PWV values over various horizontal distances at 17:25 LST (Fig. 9). The areal average of the reference PWV values became maximum when the reference PWV values were averaged within a circle of 1 km radius centered on the station 0649 and became smaller as the radius of the circle became larger. PWV_Q (66.05 mm) was 3.17 mm larger than PWV_G (62.88 mm) at 17:25 LST. PWV_G was the closest to the average of the reference PWV value within a circle centered on the station 0649 with a diameter of 27.0 km. On the other hand, PWV_Q was the closest to the reference PWV value at the station 0649.This result is consistent with the estimation of the spatial resolution of PWV using the scale height of water vapor, although it should be noted that these estimated resolutions are based on simple approximations. These results suggest that the horizontal resolution of PWV can be significantly improved using a dense network of GNSS receivers and analyzing PWV_Q when water vapor fields around receivers are fluctuated by a thunderstorm.

5. Discussion

From the simulation results described in Section 4, we found that the spatial resolution of PWV could be improved by estimating PWV using slant information at high elevation angles (e.g., by using QZSS). However, the satellite geometries used in this simulation are only a tiny fraction of all the possible geometries. If the slant path geometry used in the estimation of PWV is changed, the result also changes significantly. Therefore, we need to perform additional simulations to obtain a more generalized result by hypothesizing various satellite geometries observing the same water vapor field.

Thirty sets of satellite geometries were obtained on

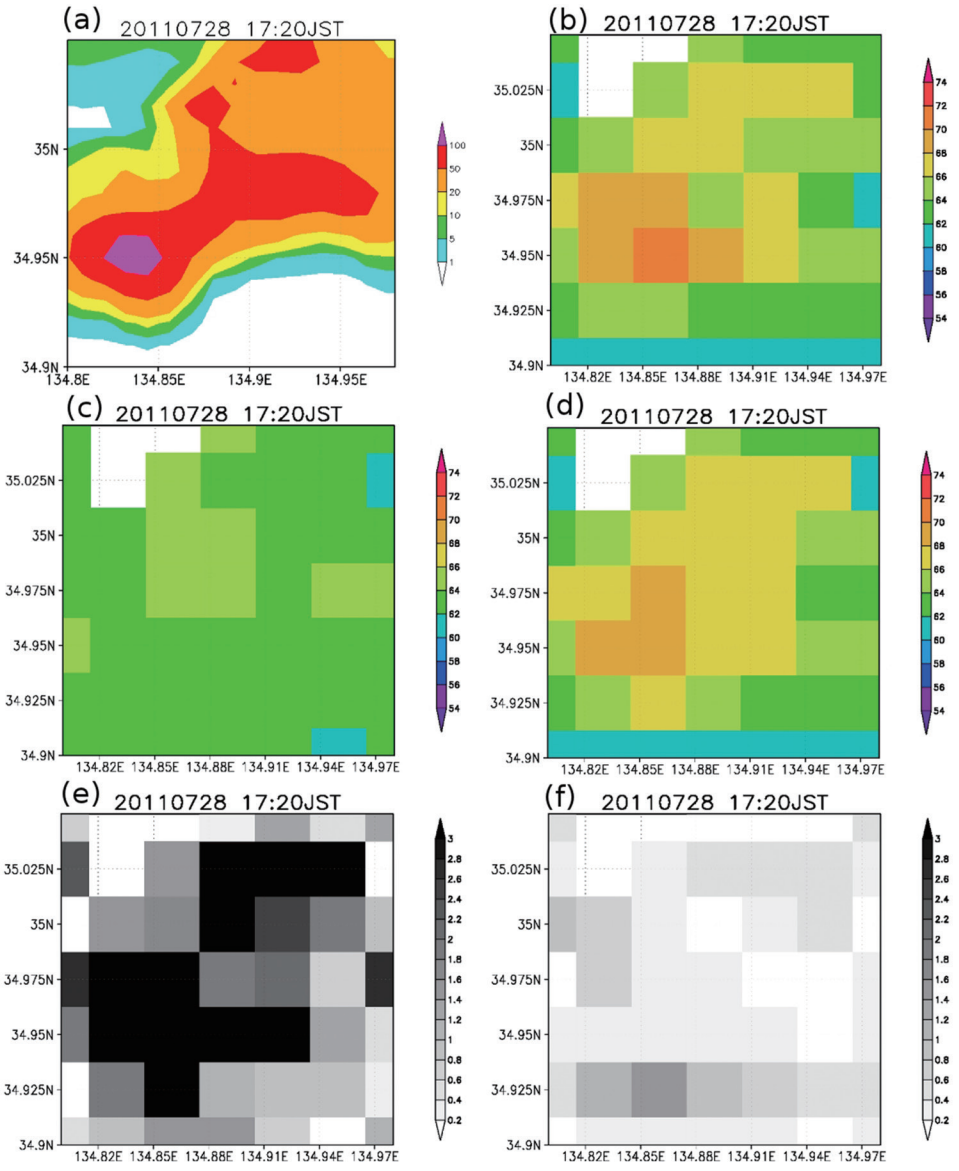

Fig. 8. (a) Horizontal distribution of precipitation intensity (mm h^{-1}) at 17:20 LST. (b), (c) and (d) are horizontal distribution of PWV (mm) of the reference value of the model, PWV_G and PWV_Q, respectively. (e) and (f) are the horizontal distribution of RMSE (mm) of PWV_G and PWV_Q, respectively.

the basis of actual orbital data every 45 min from 0:40 UTC to 22:30 UTC on 28 July 2011. These geometries cover well the possible satellite distributions because the GPS satellite geometry is repeated with the cycle of about a day. We can see an example of about 45-min variation of GNSS satellite geometry in Fig.7. As we can see in the left-side figures, at 17:00 LST, there were three GPS slant paths at low elevation angles, pointing northwest, west–southwest, and south–southwest, respectively. The elevation angles of these slant paths became smaller than 10°, and they disappeared from the figure at 17:40 LST. Another GPS satellite rose from the east during this period.

Thirty PWV values (PWV_G, PWV_Q and PWV_{HG}) were analyzed from the same water vapor field estimated by NHM at a given time using 30 different satellite geometries. By using these values, the differences of, PWV_G, PWV_Q, and PWV_{HG} from the

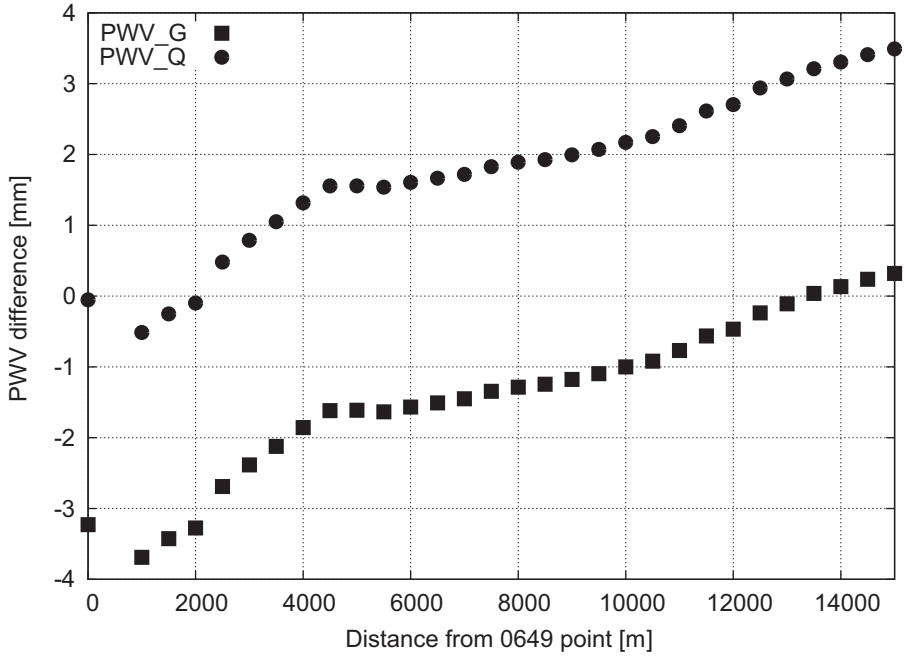

Fig. 9. Vertical axis indicates PWV (PWV_G (mark ■), and PWV_Q (mark ●)) difference from the spatially averaged model reference PWV values at the station 0649 at 17:25 LST. Spatial averaged PWV values were estimated over a variety of horizontal distances from the station 0649 which are indicated by horizontal axis.

reference PWV values were evaluated in terms of the mean difference (μ), standard deviation (σ), and RMSE, which were averaged over the 30 satellite geometries to support the results detailed in Section 4. This experiment was performed at 16:30 LST (1 h before the start of the rainfall), 17:00 LST (30 min before the start of the rainfall), 17:25 LST (5 min before the start of the rainfall), and 17:40 LST (10 min after the start of the rainfall) at the location of station 0649.

At 16:30 LST, both μ and σ of each PWV method were not so large (Table 2), because the atmospheric state near the receiver was steady (Fig. 7). Basically, the μ value of PWV_G tended to be larger than those of PWV_Q and PWV_{HG} because it contained SWV information at low elevation angle, which pass through lower humid layer. Therefore, the μ value of PWV_G was the largest at 16:30 LST.

At 17:00 LST, the rainfall system further approached the receiver from north, and the water vapor mixing ratio on the north side of the receiver became larger (Fig. 7). In this water vapor distribution, it is expected that the μ of PWV_{HG} and PWV_Q was smaller than that of PWV_G because more than one path of PWV_G penetrated the lower humid regions. As for the standard deviation, the σ value of PWV_G is expected to not have a large value because the averaging procedure of SWV, of which paths point various directions, reduces σ. The results are shown in Table 2. The μ of PWV_{HG} (0.37 mm) was smaller than that of PWV_G (0.53 mm) and larger than that of PWV_Q (−0.11 mm), and the σ of PWV_G (0.55 mm) is smaller than that of PWV_{HG} (0.60 mm). The difference between the μ of PWV_{HG} and that of PWV_Q is comparable to the difference between the μ of PWV_{HG} and that of PWV_G. It is deduced that some paths of PWV_{HG} that passed the lower humid regions increased the μ of PWV_{HG}, even if the highest elevation angles were used. These results support the aforementioned inference made about satellite geometries and water vapor distribution.

From 17:25 LST, the water vapor distribution near the receiver became more complicated. At 17:25 LST, PWV_G had a large negative bias, and the σ of PWV_{HG} was also as large as that of PWV_G, as explained in Section 4.

However, the differences from the reference value at 17:40 LST were inconsistent from those of 17:25 LST; that is, the differences of PWV_Q from the reference value became larger than those of PWV_{HG} (Table

Table 2. Mean difference (μ), standard deviation (σ), RMSE of the differences between PWV values (PWV_G, PWV_Q, PWV_{HG}) and the reference PWV at 16:30, 17:00, 17:25 and 17:40 LST, respectively.

16:30 LST 58.35 mm (true)	**μ**	**σ**	**RMSE**
PWV_G [mm]	0.16	0.35	0.38
PWV_Q [mm]	–0.11	0.09	0.15
PWV_{HG} [mm]	0.02	0.24	0.24
17:00 LST 61.23 mm (true)	**μ**	**σ**	**RMSE**
PWV_G [mm]	0.53	0.55	0.77
PWV_Q [mm]	–0.11	0.10	0.14
PWV_{HG} [mm]	0.37	0.60	0.71
17:25 LST 66.11 mm (true)	**μ**	**σ**	**RMSE**
PWV_G [mm]	–2.72	0.58	2.78
PWV_Q [mm]	–0.08	0.10	0.13
PWV_{HG} [mm]	–0.21	0.55	0.59
17:40 LST 63.23 mm (true)	**μ**	**σ**	**RMSE**
PWV_G [mm]	–0.76	0.43	0.88
PWV_Q [mm]	–0.12	0.39	0.41
PWV_{HG} [mm]	–0.30	0.73	0.79

1). To show why these differences were caused, water vapor and path distributions (Fig. 7) were mentioned again. There was a relatively dry region just south of the receiver, and the path of QZSS passed this region, while the path of GPS with the highest elevation angle stayed in the humid region. Therefore, the difference of PWV_{HG} from the reference value was the smallest although the elevation angle of QZSS might be higher than that of PWV_{HG} . To confirm whether this situation is general, the μ and σ of PWV_Q and RMSE were also evaluated. When 30 geometries of the satellites were used, both μ and σ of PWV_Q were the smallest. The RMSE of PWV_Q was also the smallest at all times, and the RMSE of PWV_{HG} was smaller than that of PWV_G. This result indicates that RMSE from PWV reference is significantly influenced by the distributions of water vapor and paths and that the situation in which the RMSE of PWV_{HG} was the smallest is not general. Bevis et al. (1992) showed that GPS-derived PWV agreed with microwave radiometer measurements within 2 mm in RMSE. Shoji et al. (2004) and Sato et al. (2013) reported that validation results of PWV estimated by PPP against radiosonde and microwave radiometer had an RMSE difference of less than or equal to 2.0 mm. These results were not necessarily observed under meso-γ scale disturbances, and it is expected that the RMSE of PWV in real observations will be larger in case of highly variable spatial distributions of water vapor around the receiver. It is also worth noting that these comparison results are not equal to the discrepancy between the vertically integrated water vapor amount and GPS-derived PWV because radiosondes are advected by winds; when they are advected far away from the launching site, radiosonde-derived PWV may significantly differ from the vertically integrated water vapor amount at the launching site (Sato et al. 2013).

From these additional four simulations (16:30 LST, 17:00 LST, 17:25 LST, and 17:40 LST), we got more generalized results that PWV_Q provides the most accurate and precise information about the local PWV distribution before and after the rainfall started.

6. Summary

The spatial distribution of PWV during heavy rainfall was evaluated using the output of the JMA non-hydrostatic model (NHM). The evaluation was performed on GNSS-derived PWV values obtained

by simulating three different retrieval methods: using all GPS satellites above an elevation angle higher than 10° (PWV_G), using only the QZSS satellite at the highest elevation (PWV_Q), and using only the GPS satellite at the highest elevation (PWV_{HG}).

The NHM output with a horizontal grid interval of 1 km was used, in which a rainfall system generated north of receiver moved southwards and passed over the receiver position. The satellite apparent trajectories used in this simulation were computed using observed GPS data at a GEONET station; the apparent trajectories of four QZSS satellites were also computed on the basis of the assumption that four QZSS satellites will be available in the near future.

During a period with fluctuations in the water vapor field from 20–30 min before the rain started to the end of the precipitation, the RMSE of PWV_G with respect to the reference PWV was 1.82 mm and 1.37 mm at the NHM model points corresponding to GEONET stations 0347 and 0649, respectively. In contrast, the RMSE of PWV_Q was 0.46 mm and 0.29 mm, respectively, at the same two points, during the same period. The PWV_{HG} time series had a discontinuity (~ 2 mm) when the GPS satellite at the highest elevation angle changes, whereas the discontinuity in the PWV_Q time series was small because the elevation angle at which the replacement of the highest-elevation QZSS satellite occurs was much higher (i.e., with lower azimuth difference). Although the differences between the reference PWV value (by the NHM model) and the PWV values estimated by all three methods were small 1 h before the rainfall started, PWV_G showed a larger difference 30 min before the rain. This is because a slant path at low elevation pointing north passed through a humid region associated with the rainfall system that was approaching the receiver from north. A large underestimation of PWV_G occurred 5 min before the rainfall because the top height of the moist layer over 0.001 kg kg^{-1} water vapor mixing ratio was relatively higher just over the location of the receiver; this event was attributed to deep convection. Differences of PWV_{HG} and PWV_Q from the reference PWV values were smaller than that of PWV_G. PWV_{HG} may be more suitable in the places where QZSS is not available or when other GNSS satellites (GPS, GLONASS, BeiDou, Galileo, etc.) are actually higher than the QZSS satellites (although this might introduce discontinuities).

When PWV_G and PWV_Q data were applied to the observation of meso-γ scale (2–20 km) distribution of water vapor in the NHM model with inter-station distances equal to 2.7 km along longitudinal and latitudinal lines, PWV_G could not capture the complicated PWV fluctuations associated with a thunderstorm, because PWV_G produces smoothed value due to the mapping and averaging of all the slant water vapor values above an elevation angle of 10°. In contrast, PWV_Q captured the PWV fluctuations. Spatial resolutions of PWV_G and PWV_Q are simply estimated as about 30 km and 1 km because the average scale height of water vapor during the disturbed period around the station 0649 was 2.75 km, and elevation cutoff angles of PWV_G and PWV_Q were assumed as 10° and 80°, respectively. This estimation was consistent with the validation result by using NHM output. Therefore, PWV_G has the potential to improve the horizontal resolution of PWV to less than 2.7 km during heavy rainfall.

Thirty different satellite geometries were simulated and applied to the same water vapor field to increase the redundancy of the resulting data. The reliability of the three different GNSS-derived PWV retrieval methods was evaluated by means of their difference with respect to the reference PWV produced by the NHM model, expressed in terms of mean (μ), standard deviation (σ) and RMSE. In this experiment, the μ of PWV_G was improved by estimating PWV from the SWV of a single high-elevation satellite: PWV_G and PWV_{HG}. The σ of PWV_Q was smaller than that of PWV_G and PWV_{HG}, which significantly vary depending on satellite geometry. It was found that PWV_Q is the most accurate and precise method to retrieve water vapor from GNSS measurements, not depending on satellite geometry.

Acknowledgments

The JMANHM model used in this study was provided by the Meteorological Research Institute (MRI).The initial and boundary data of JMANHM used in this study were provided by means of the "Meteorological Research Consortium", a framework for research cooperation of the JMA and Meteorological Society of Japan (MSJ). The authors would like to express their gratitude to Dr. Yoshinori Shoji and Dr. Takuya Kawabata of the MRI for their support to use the JMANHM model. Thanks are extended to Dr. Kazutoshi Sato of the Center for the Promotion of Interdisciplinary Education Research (CPIER, Kyoto University), and to the other members of Tsuda laboratory of RISH, who provided us with useful comments.

References

Bevis, M., S. Businger, T. A. Herring, C. Rocken, R. A.

Anthes, and R. H. Ware, 1992: GPS Meteorology: Remote sensing of atmospheric water vapor using or estimation of the wet delay. *J. Geophys. Res.*, **97**, 15787–15801.

Elgered, G., J. M. Johansson, B. O. Ronnang, and J. L. Davis, 1997: Measuring regional atmospheric water vapor using the Swedish permanent GPS network. *Geophys. Res. Lett*., **24**, 2663–2666.

Gutman, S. I., S. Sahm, S. G. Benjamin, B. E. Schwartz, K. Holub, J. Q. Stewart, and T. L. Smith, 2004: Rapid retrieval and assimilation of ground based GPS precipitable water observations at the NOAA forecast systems laboratory: Impact on weather forecasts. *J. Meteor. Soc. Japan*, **82**, 351–360.

Gendt, G., G. Dick, C. Reigber, M. Tomassini, Y. Liu, and M. Ramatschi, 2004: Near real time GPS water vapor monitoring for numerical weather prediction in Germany. *J. Meteor. Soc. Japan,* **82**, 361–370.

Ishikawa, Y., 2010: The use of ground based GPS data for Meso-scale analysis. *Suchi Yohoka Hokoku Bessatsu* (Additional Volume to Report of Numerical Prediction Division), **56**, 54–60 (in Japanese).

Iwabuchi, T., I. Naito, S. Miyazaki, and N. Mannoji, 1997: Precipitable water vapor moved along a front observed by the nationwide GPS network of geographical survey institute. *Tenki*, **44**, 765–766 (in Japanese).

Iwabuchi, T., Y. Shoji, S. Shimada, and H. Nakamura, 2004: Tsukuba GPS dense net campaign observation: Comparison of stacking maps of post-fit phase residuals estimated from three software packages. *J. Meteor. Soc. Japan*, **82**, 315–330.

Japan Meteological Agency, 2013: Outline of the operational numerical weather prediction at the Japan Meteorological Agency. *WMO Technical Progress Report on the Global Data Processing and Forecasting System (GDPFS) and Numerical Weather Prediction (NWP) Research.*, 28–36.

Kain, J., and J. Fritsch, 1993: Convective parameterization for mesoscale models: The Kain–Fritsch scheme. *The representation of cumulus convection in numerical models. Meteor. Monogr.,* **46**, 165–170.

Kawabata, T., H. Seko, K. Saito, T. Kuroda, K. Tamiya, T. Tsuyuki, T. Honda, and Y. Wakazki, 2007: An assimilation and forecasting experiment of the Nerima heavy rainfall with a cloud-resolving 4-dimentional variational data assimilation system. *J. Meteor. Soc. Japan*, **85**, 255–276.

Kuo, Y.-H., Y.-R. Guo, and R. Westwater, 1993: Assimilation of precipitable water measurements into a mesoscale numerical mode. *Mon. Wea. Rev*., **121**, 1215–1238.

MacMillan, D. S., 1995: Atmospheric gradients from very long baseline interferometry observations. *Geophys. Res. Lett*., **22**, 1041–1044.

Niell, A. E., 1996: Global mapping functions for the atmosphere delay at radio wavelengths. *J. Geophys. Res.*, **101**, 3227–3246.

Saito, K., J. Ishida, K. Aranami, T. Hara, T. Segawa, M. Narita, and Y. Honda, 2007: Nonhydrostatic atmospheric models and operational development at JMA. *J. Meteor. Soc. Japan,* **85B**, 271–304.

Sato, K., E. Realini, T. Tsuda, M. Oigawa, Y. Iwaki, Y. Shoji, and H. Seko, 2013: A high-resolution, precipitable water vapor monitoring system using a dense network of GNSS receivers. *Journal of Disaster Research*, **8**, 37–47.

Seko, H., T. Kawabata, T. Tsuyuki, H. Nakamura, K. Koizumi, and T. Iwabuchi, 2004a: Impacts of GPS-derived water vapor and radial wind measured by Doppler radar on numerical prediction of precipitation. *J. Meteor. Soc. Japan*, **82**, 473–489.

Seko, H., N. Nakamura, Y. Shoji, and T. Iwabuchi, 2004b: The Meso-γ scale water vapor distribution associated with a thunderstorm calculated from a dense network of GPS receivers. *J. Meteor. Soc. Japan*, **82**, 569–586.

Seko, H., H. Nakamura, and S. Shimada, 2004c: An evaluation of atmospheric models for GPS data retrieval by output from a numerical weather model. *J. Meteor. Soc. Japan*, **82**, 339–350.

Shoji, Y., H. Nakamura, T. Iwabuchi, K. Aonashi, H. Seko, K. Mishima, A. Itagaki, R. Ichikawa, and R. Ohtani, 2004: Tsukuba GPS dense net campaign observation: Improvement in GPS analysis ofslant path delay by stacking one-way postfit phase residuals. *J. Meteor. Soc. Japan*, **82**, 301–314.

Shoji, Y., 2013: Retrieval of water vapor inhomogeneity using the Japanese nationwide GPS array and its potential for prediction of convective precipitation., *J. Meteor. Soc. Japan*, **91**, 43–62.

Smith, T. L., S. G. Benjamin, B. E. Schwartz, B. E., and S. I. Gutman, 2000: Using GPS-IPW in a 4-D data assimilation system. *Earth Planets Space*, **52**, 921–926.

Thayer, D., 1974: An improved equation for the radio refractive index of air. *Radio Sci*., **9**, 803–807.

Tsuda, T., K. Heki, S. Miyazaki, K. Aonashi, K. Hirahara, M. Tobita, F. Kimara, T. Tabei, T. Matsushima, F. Kimura, M. Satomura, T. Kato, and I. Naito, 1998: GPS meteorology project of Japan—exploring frontiers of geodesy. *Earth Planets Space,* **50**, i–iv.

Rocken, C., R. Ware, T. Van Hove, F. Solheim, C. Alber, J. Johnso, M. Bevis, and S. Businger, 1993: Sensing atmospheric water vapor with the global positioning system. *Geophys. Res. Lett.*, **20**, 2631–2634.